ACS APPLIED MATERIALS & INTERFACES

www.acsami.org

Research Article

Multimaterial Three-Dimensional Printing of Ultraviolet-Curable Ionic Conductive Elastomers with Diverse Polymers for Multifunctional Flexible Electronics

Xiangnan He,[#] Jianxiang Cheng,[#] Zhenqing Li, Haitao Ye, Xinfeng Wei, Honggeng Li, Rong Wang, Yuan-Fang Zhang, Hui Ying Yang, Chuanfei Guo, and Qi Ge*

Cite This: *ACS Appl. Mater. Interfaces* 2023, 15, 3455−3466

ABSTRACT: Ionic conductive elastomers (ICEs) are emerging stretchable and ionic conductive materials that are solvent-free and thus demonstrate excellent thermal stability. Three-dimensional (3D) printing that creates complex 3D structures in free forms is considered as an ideal approach to manufacture sophisticated ICE-based devices. However, the current technologies constrain 3D printed ICE structures in a single material, which greatly limits functionality and performance of ICE-based devices and machines. Here, we report a digital light processing (DLP)-based multimaterial 3D printing capability to seemly integrate ultraviolet-curable ICE (UV-ICE) with nonconductive materials to create ionic flexible electronic devices in 3D forms with enhanced performance. This unique capability allows us to readily manufacture various 3D flexible electronic devices. To demonstrate this, we printed UV-ICE circuits into polymer substrates with different mechanical properties to create resistive strain and force sensors; we printed flexible capacitive sensors with high sensitivity (2 kPa^{-1}) and a wide range of measured pressures (from 5 Pa to 550 kPa) by creating a complex microstructure in the dielectric layer; we even realized ionic conductor-activated four-dimensional (4D) printing by printing a UV-ICE circuit into a shape memory polymer substrate. The proposed approach paves a new efficient way to realize multifunctional flexible devices and machines by bonding ICEs with other polymers in 3D forms.

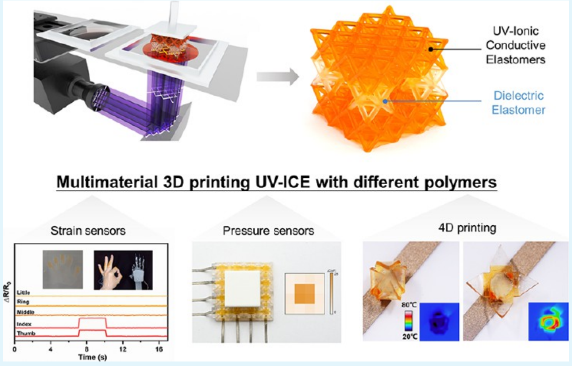

KEYWORDS: *flexible electronics, ionic conductive elastomers, multimaterial 3D printing, digital light processing, 4D printing*

1. INTRODUCTION

Flexible electronics have attracted wide attention because of their impactful applications in electronic skin,[1,2] energy harvesting and storage devices,[3,4] human motion detectors,[5,6] health monitoring systems,[7−9] and soft robots.[10] Stretchable conductors are crucial for enabling flexible electronics that are able to not only receive and transport electronic signals but also conform large deformations. To date, there are two mainstream strategies for achieving stretchable conductors: strain engineering and nanocomposites.[11] In the first strategy, the non-stretchable but conductive materials, such as metals, need to be engineered to special mechanical structures or architectures, such as out-of-plane wrinkles,[12] in-plane serpentines,[13] and kirigami architectures,[14] to enable high stretchability of whole structures while maintaining local deformations at a low strain level. However, this strategy requires sophisticated structural designs and a series of complicated manufacturing processes. The second strategy is to embed conductive fillers, such as carbon nanotubes,[15] silver nanowires,[16] and metal nanoparticles[17] or flakes,[18] into a dielectric elastomeric matrix to form nanocomposites for releasing stretchable conductors. Nevertheless, due to the percolation-dependent conductivity, the stretchable conductors are highly strain sensitive and not stable after multiple strain cycles.[11]

Compared with traditional electronic conductors, ionic conductors use ions as current carriers and have recently enabled a new family of devices called ionotronics.[19−21] Among all the ionic conductors, hydrogels contain large amounts of water that can dissolve ions and therefore have been widely used to realize various applications including hydrogel sensors,[22] electronic devices,[23,24] batteries,[25] actuators,[26] and soft robots.[27] However, the use of hydrogels as conductors for flexible electronics encounters one significant challenge—dehydration. Encapsulating hydrogels into anti-

Received: October 21, 2022
Accepted: November 30, 2022
Published: December 20, 2022

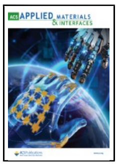

https://doi.org/10.1021/acsami.2c18954

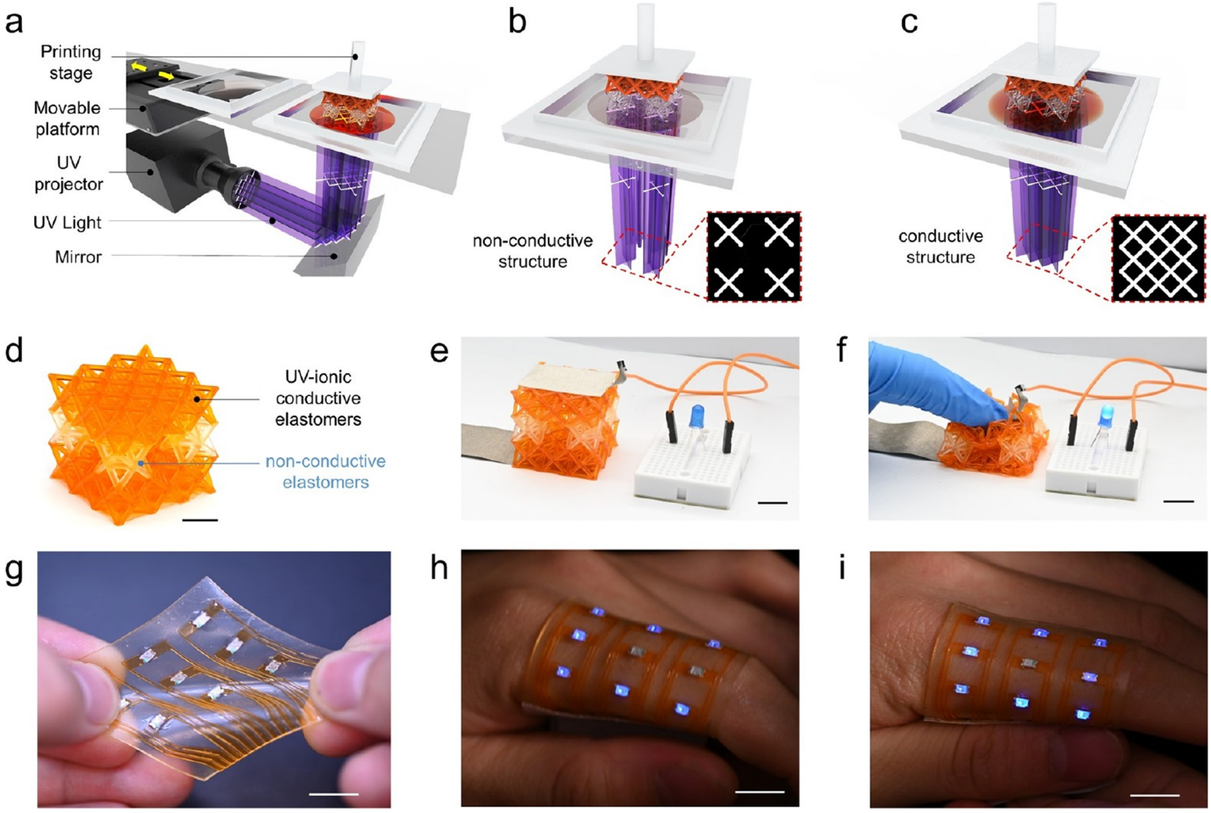

Figure 1. Multimaterial 3D printing UV-ICEs with nonconductive elastomers. (a) Illustration of the DLP-based multimaterial 3D printing system. (b, c) Processes of printing UV-ICE and nonconductive elastomer structures, respectively. (d) Octet truss lattice structure printed with the UV-ICE and nonconductive elastomer. Scale bar: 10 mm. (e, f) Photographs of an Octet truss lattice structure before and after compressing. Scale bar: 10 mm. (g) A stretchable multimaterial 3D printing circuit with a patch LED. Scale bar: 10 mm. (h, i) A functional LED array wrapped around a human finger with different patterns. Scale bar: 10 mm.

dehydration elastomeric layers has successfully addressed this issue,[28−30] but also complicated the fabrication process and constrained the geometry hydrogel-based flexible electronics to laminate structures.

Ionic conductive elastomers (ICEs) are emerging ionic conductive materials that are solvent-free[31−33] and thus demonstrate not only decent stretchability and conductivity but also excellent thermal stability. These remarkable properties make ICEs ideal materials for engineering ionic devices including touch sensors,[34,35] ionic skin,[36] and triboelectric nanogenerators.[37] However, the current manufacturing of ICEs mainly relies on molding and casting methods that constrain the manufactured ionic devices to simple and large bulk geometries consisting of a single material. Three-dimensional (3D) printing that creates complex 3D objects in free forms is considered as an ideal approach to manufacture more sophisticated ionic devices. Digital light processing (DLP)-based 3D printing creates complex 3D structures with high resolutions through digitalized ultraviolet (UV) projection that triggers localized photopolymerization, converting liquid polymer solution to solid 3D structures. Recently, researchers have developed UV-curable ICEs, which is compatible with DLP-based 3D printing to form 3D flexible tactile sensors with high sensitivity.[33] However, the current printed ICE sensors are fabricated with a single material or in a simple laminate form that was not fully printed.

Here, we report a DLP-based multimaterial 3D printing capability to seemly integrate ICE with nonconductive materials to create ionic flexible electronic devices in 3D forms with enhanced performance. We develop ultraviolet-curable ionic conductive elastomers (UV-ICEs) that are not only highly stretchable (elongation at break: up to 1300%) but also compatible with DLP-based 3D printing to create highly complex ionic conductive 3D structures with high resolution (up to 5 μm). More importantly, the UV-ICEs are able to form a mechanically robust interface with diverse UV-curable but nonconductive materials ranging from soft elastomers to rigid polymers. This unique property allows us to use a self-built DLP-based multimaterial 3D printer to readily manufacture various flexible electronic devices consisting of ICE-based circuits and various nonconductive polymers. We printed a flexible smart glove consisting of UV-ICE circuits into a soft substrate to collect bending signals of finger motions that were later used to manipulate a robotic hand. By printing a UV-ICE circuit into a polymer substrate with various stiffness, we created force sensors that can measure an axial force of up to 100 N. We also 3D printed flexible capacitive sensors with high sensitivity (2 kPa^{-1}) and a wide range of measured pressures (from 5 Pa to 550 kPa) by creating a complex microstructure in the dielectric layer. We can even print a flexible pressure sensor array that is able to map pressure distribution. Moreover, for the first time, we demonstrate ionic conductor-activated four-dimensional (4D) printing by printing a UV-ICE circuit into a shape memory polymer substrate. The proposed approach paves a new efficient way to fabricate flexible electronics with greatly extended functionality and performance through DLP-based multimaterial 3D printing.

https://doi.org/10.1021/acsami.2c18954
ACS Appl. Mater. Interfaces 2023, 15, 3455−3466

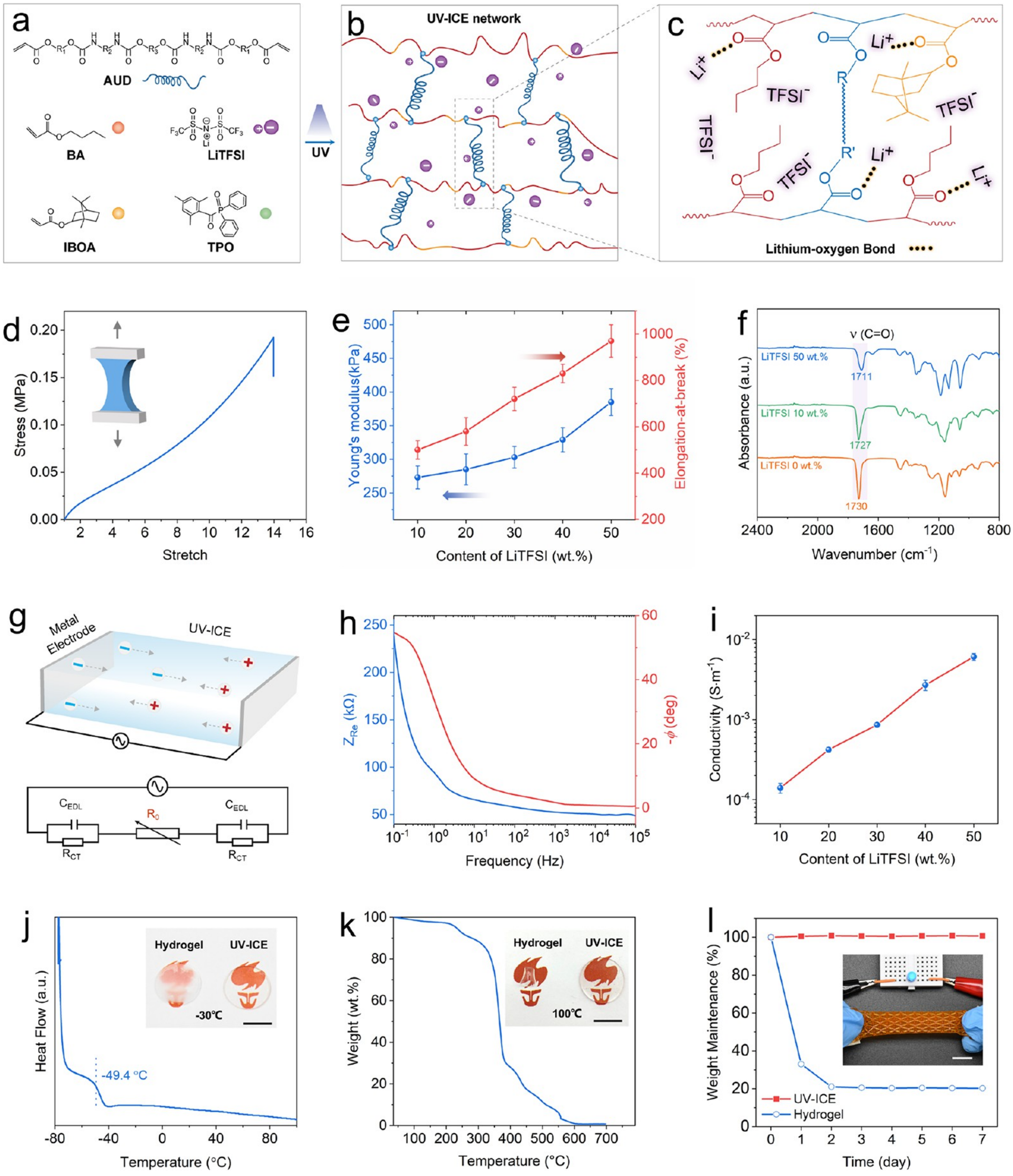

Figure 2. Synthesis and properties of UV-ICE. (a) Detailed chemical structures of BA, AUD, IBOA, LiTFSI, and TPO that are used to prepare the UV-ICE precursor solution. (b) UV-ICE network structure after 3D printing. (c) Detailed chemical structure of crosslinked UV-ICE. (d) Stress−strain behavior of the UV-ICE. (e) Effect of LiTFSI content on Young's modulus and elongation at break of the UV-ICE. (f) FTIR spectrum of the UV-ICE with different LiTFSI contents. (g) Illustration of the electrical performance test of the UV-ICE. (h) Plot of real part Z_{Re} and negative phase angle versus testing frequency for the UV-ICE. (i) Ionic conductivity of the UV-ICE with different LiTFSI contents. (j) DSC curves of the UV-ICE. The inset pictures were the UV-ICE and PAAm hydrogel after being stored at −30 °C for 15 min. Scale bar: 10 mm. (k) Thermogravimetric curves of the UV-ICE. The inset pictures were the UV-ICE and PAAm hydrogel after being stored at 100 °C for 20 min. Scale bar: 10 mm. (l) Weight change of UV-ICE samples and PAAm hydrogel samples in a week. The inset picture was the printed UV-ICE structure after being stored at room temperature for a week. Scale bar: 10 mm.

2. RESULTS AND DISCUSSION

2.1. Multimaterial 3D Printing UV-ICEs with Nonconductive Elastomers. Figure 1 presents the ionic flexible electronic structures and devices that are fabricated on a self-built DLP-based multimaterial 3D printing system. Figure 1a−c shows the process of printing a multimaterial Octet truss where the top and bottom layers made of UV-ICE are connected with a middle layer made of a nonconductive elastomer. Figure 1a illustrates the multimaterial 3D printing system that adopts "bottom-up" projection configuration where UV patterns are irradiated from the UV projector positioned below the printing stage that moves vertically to control the thickness of each printed slice. Between the printing stage and the UV projector, there is a movable platform that supports two polymer solution containers and moves horizontally to deliver the needed polymer precursor solution for the corresponding slice. As shown in Figure 1b, when a slice of the nonconductive elastomer part is being printed, the transparent nonconductive elastomer precursor solution moves below the printing stage, and the corresponding UV pattern is illuminated into the precursor solution. In Figure 1c, when a layer of the UV-ICE part is being printed, the orange UV-ICE precursor solution is positioned below the printing stage, and the corresponding UV pattern is irradiated into the orange solution. Figure 1d presents the printed Octet truss lattice structure. In Figure 1e, we attach two electrodes to the Octet truss's top and bottom surfaces made of UV-ICE to create a circuit that is initially not conductive. Under compression, the two conductive layers contact to make the circuit conductive that is indicated by the turned-on light-emitting diode (LED) bulb (Figure 1f).

The DLP-based multimaterial 3D printing system enables the precise arrangement of UV-ICE and other nonconductive polymers in a 3D space and allows us to fabricate various flexible electronic devices in a single printing process. As shown in Figure 1g, we print a flexible circuit board consisting of UV-ICE circuit patterns on an elastomeric substrate and exhibiting good stretchability with a 3 × 3 LED array attached on it. The nine circuits allow us to independently control the nine LED bulbs. Figure 1h,i demonstrates that the LED array displays letters "C" and "O" by selectively turning on and off the nine individual LED bulbs.

2.2. Synthesis and Properties of UV-ICE.

Figure 2a presents the chemicals that are used to prepare the UV-ICE precursor solution that consists of butyl acrylate (BA) as the monomer, aliphatic urethane diacrylate (AUD) as the crosslinker that is diluted by 33 wt % isobornyl acrylate (IBOA), and 2,4,6-trimethylbenzoyl diphenylphosphine oxide (TPO) as the photoinitiator. Moreover, lithium bis(trifluoromethane sulfonimide) (LiTFSI), as the electrolyte salt, needs to be dissolved into the UV-ICE precursor solution to impart ionic conductivity. Figure 2a–c illustrates the photopolymerization of the UV-ICE system during DLP-based 3D printing. Irradiation of UV lights activates the TPO photoinitiator to generate free radicals that propagate through BA, IBOA, and AUD molecules (Figure 2a) that are chemically crosslinked to form covalent networks (Figure 2b) where the detailed chemical structure is presented in Figure 2c. In the UV-ICE, lithium ions coordinate with oxygen atoms on ester groups in polymer chains to form lithium–oxygen (Li–O) bonds.[38,39] Under the applied electric field, lithium ions migrate within the UV-ICE network, thereby imparting ionic conductivity to the UV-ICE system.

The UV-ICE is highly stretchable and can be stretched by ~1300% (Figure 2d). As the stretchability of UV-ICE determines the deformation capacity of 3D printed objects, we performed uniaxial tensile tests on the UV-ICE system to study the effect of AUD and LiTFSI contents on the stress–strain behavior of the system. As presented in Figure S1, the increase in the AUD content from 10 to 50 wt % results in an enhancement in Young's modulus from 55 to 630 kPa and a gradual decrease in the elongation at break from 930 to 420%. Thus, the mechanical property of the UV-ICE can be adjusted by tuning the crosslinker content. In contrast to the effect of AUD, adding more LiTFSI leads to the increase in both Young's modulus and elongation at break (Figure 2e and Figure S2). This phenomenon is attributed to the Li–O bonds between lithium ions and carbonyl oxygen atoms on polymer chains.[40] We performed Fourier transform infrared (FTIR) spectroscopy to validate this explanation. As shown in Figure 2f, the C=O group stretching of the pure BA–AUD (LiTFSI content: 0 wt %) sample is at 1730 cm^{-1}, and the increase in the LiTFSI content shifts the C=O group stretching to a lower wavenumber due to the presence of Li–O bonds, as illustrated in Figure 2c. In addition to the high stretchability, the UV-ICE sample also exhibits excellent mechanical repeatability. As shown in Figure S3, no fracture or obvious stress decay is observed after the UV-ICE sample was cyclically stretched from 0 to 200% 1000 times. The loading–unloading curves in Figure S4 demonstrate the low hysteresis effect of the UV-ICE sample when the tensile strain is more than 200%.

We investigate the ionic conductivity of the UV-ICE system by measuring alternating-current impedance spectroscopy on an electrochemical workstation. As illustrated in Figure 2g, two silver fabrics are attached to the two ends of the UV-ICE sample. In an equivalent circuit, the ICE part is modeled as a pure resistance, R_0, and the end of the ICE sample can be modeled by using the Randles circuit model consisting of a capacitor, C_{EDL}, in parallel with a resistor, R_{CT}.[41] Here, C_{EDL} is attributed to the electric double layer (EDL) forming at the interface between the ICE sample and the silver fabric, and R_{CT} is the charge transfer resistance. According to the equivalent circuit model, we can calculate the impedance between the two silver fabrics and the UV-ICE sample as

$$\mathbf{Z} = Z_{\text{Re}} + Z_{\text{Im}}\mathbf{i} \text{ with } Z_{\text{Re}} = \frac{2R_{\text{CT}}}{1 + (2\pi f C_{\text{EDL}} R_{\text{CT}})^2} + R_0,\ Z_{\text{Im}} = -\frac{4\pi f C_{\text{EDL}} R_{\text{CT}}^2}{1 + (2\pi f C_{\text{EDL}} R_{\text{CT}})^2} \quad (1)$$

where f is the testing frequency and the real part Z_{Re} of $\mathbf{Z}$ is the resistance between the two silver fabrics. As presented in Figure 2h, the measured real part Z_{Re} of UV-ICE is a function of testing frequency f: at a low-frequency range (0.1–100 Hz), Z_{Re} decreases with the increase in f and the negative phase angle $-\phi$ ($\tan\phi = Z_{\text{Im}}/Z_{\text{Re}}$) is nonzero due to the effect of the EDL forming at the interface between the UV-ICE sample and the silver fabrics,[41] while at a high-frequency range (100 Hz to 10 kHz), the effect of EDL becomes negligible, Z_{Re} reaches a minimum and stable state, and $-\phi$ turns to be 0°. We further investigated electrical conductivity of the UV-ICE system. As presented in Figure 2i, the conductivity raises from 1.4×10^{-4} to 6.1×10^{-3} $\text{S}\cdot\text{m}^{-1}$ by increasing the LiTFSI content from 10 to 50 wt %. The 50 wt % is the maximum content of LiTFSI that can be dissolved in the BA–AUD solution. Moreover, Figure S5 shows that the conductivity of UV-ICE is highly temperature dependent, and it escalates by more than one order of magnitude as the temperature raises from 5 to 65 °C.

Compared with hydrogel-based ionic conductors, UV-ICEs are physically more stable within a wide temperature range. Figure 2j presents the differential scanning calorimetry (DSC) results, which indicate that the glass transition temperature (T_g) of the UV-ICE sample is −49.4 °C above which the UV-ICE sample exhibits typical rubbery mechanical behavior. As demonstrated in the inset of Figure 2j, the polyacrylamide

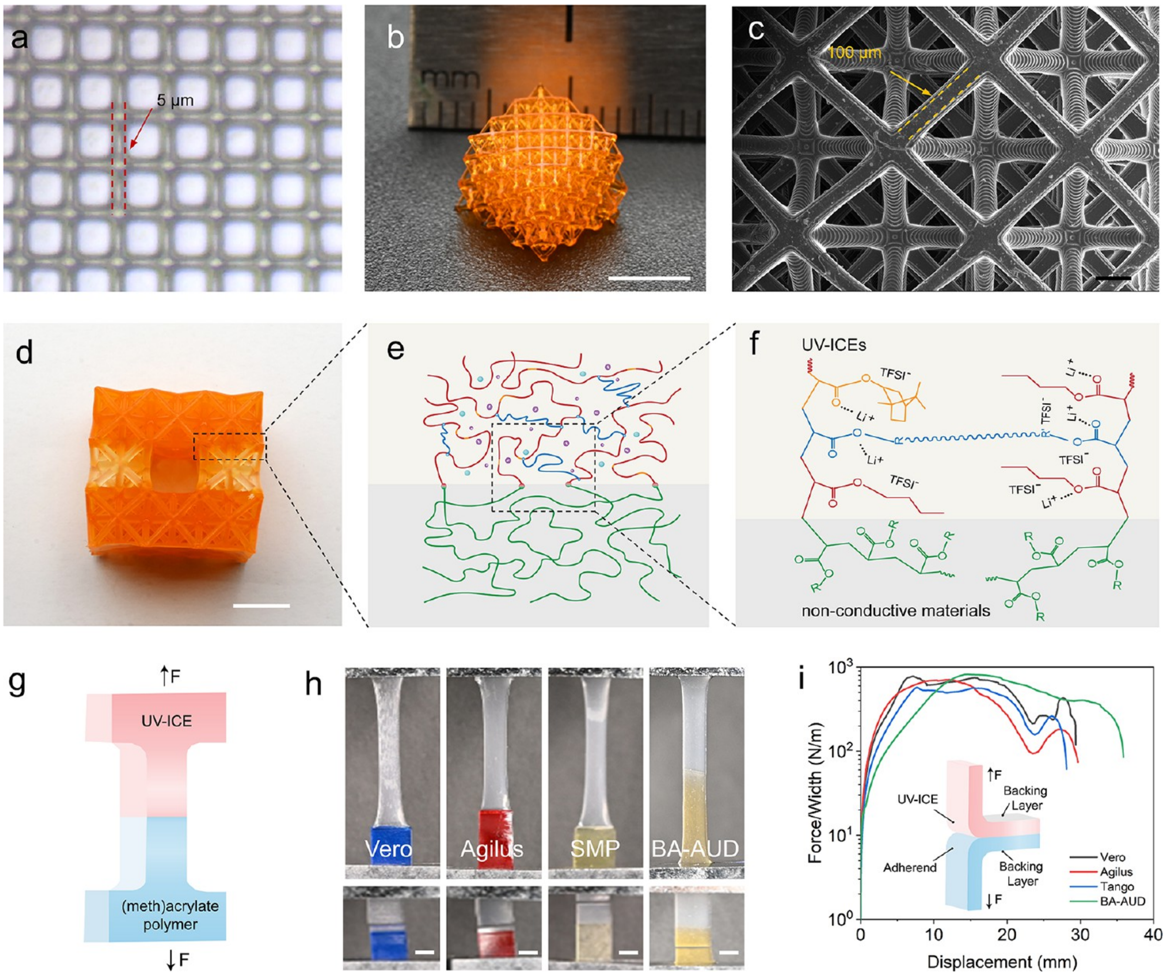

Figure 3. Characterization on 3D printing of UV-ICEs. (a) Microscopic image of the grid pattern with 5 μm width printed with the UV-ICE. (b) Octet truss structure printed with UV-ICE. Scale bar: 5 mm. (c) Scanning electron microscope (SEM) image of the Octet truss. Scale bar: 200 μm. (d) Octet truss lattice structure printed with the UV-ICE and nonconductive elastomer. Scale bar: 10 mm. (e) Schematic of the interface of UV-ICEs and nonconductive (meth)acrylate polymers. (f) Chemical covalent structures in the interface between UV-ICEs and nonconductive (meth)acrylate polymers. R is the possible middle chains in (meth)acrylate polymers. (g) Illustration of bonding UV-ICEs to (meth)acrylate polymers. (h) Uniaxial tensile tests of the dog bone samples printed with half UV-ICEs and half nonconductive (meth)acrylate polymers. The polymers in the picture from left to right respectively are the Vero, Agilus, shape memory polymer (SMP), and BA–AUD elastomer. Vero scale bar: 5 mm. (i) Force/width–displacement curves to investigate the interfacial toughness (180° peeling test).

(PAAm) hydrogel was crystallized at −30 °C after 15 min, while the UV-ICE sample remained the initial state. The thermogravimetric analyses (TGA) in Figure 2k further confirm that the UV-ICE sample is stable below 200 °C where no apparent weight loss is observed. The stability of the PAAm hydrogel and UV-ICE was compared at 100 °C in an oven. As demonstrated in the insets of Figure 2k, after 20 min at 100 °C, the UV-ICE sample was unchanged, but the PAAm hydrogel severely shrunk due to water loss. Moreover, in contrast to hydrogels, the printed UV-ICE structure had little loss of mass due to the absence of solvents and maintained excellent tensile and electrical conductivity after being left at room temperature for a week (Figure 2l). In addition, the UV-ICEs exhibit excellent stability in electronical conductivity. As shown in Figure S6, the variation in conductivity is less than 4% when the UV-ICE samples were exposed to an ordinary environment (temperature, 27 °C; humidity, 50%) for 2 weeks. We also carried out experiments to investigate the weight stability of the UV-ICEs at room temperature over 1 week. As presented in Figure S7, no weight losses were observed for all the samples with different LiTFSI contents under the humidity of 40 and 80% over 1 week. High LiTFSI content (50 wt %) makes the UV-ICE sample absorb a small amount of water.

2.3. 3D Printing of UV-ICEs.

The photopolymerizable UV-ICE system is highly suitable for DLP-based 3D printing technology. We can print structures made of UV-ICE on a high-resolution, DLP-based 3D printer that transforms liquid UV-ICE precursor solution into solid 3D structures via localized photopolymerization controlled by a high-precision UV light engine. The UV-ICE can be used to print a high-precision grid (up to 5 μm in Figure 3a) and a highly complex Octet truss lattice structure with a rod diameter of ~100 μm (Figure 3b,c). The rheological behavior of the UV-ICE system is critical to the DLP-based 3D printing process. All UV-ICE precursor solutions with different LiTFSI contents possess low viscosity (less than 0.08 Pa·s, Figure S8) at room temperature and are suitable for DLP-based 3D printing.[42] As shown in Figure S9, we performed photo-rheological characterizations to quantify the curing time required for the UV-ICE precursor solutions with different LiTFSI contents to achieve their gel points. Overall, the gelation process of UV-ICE is fast, so it requires ~4 s (~8×10^{-4} J/mm^2) to cure a 50 μm thick layer.

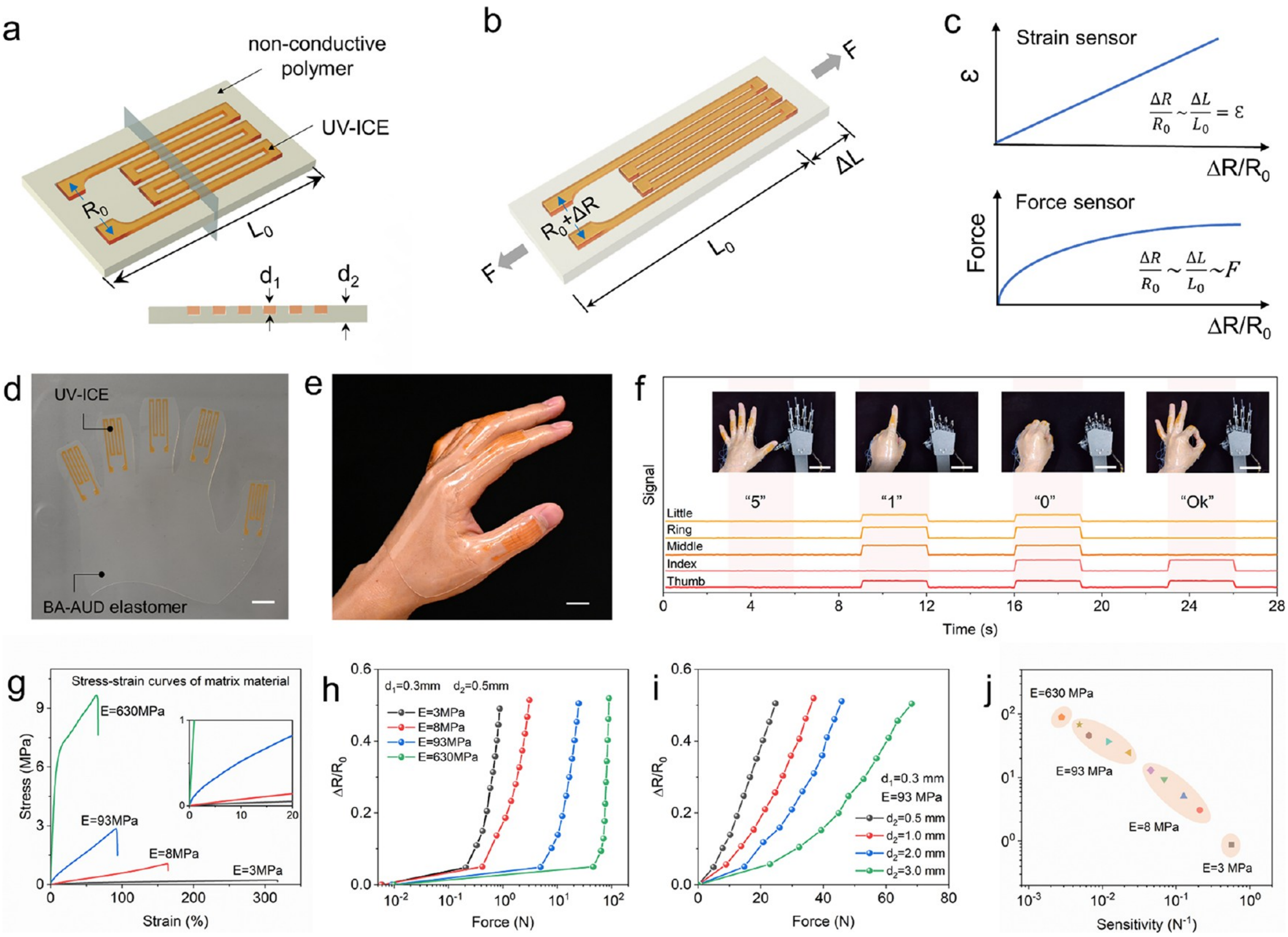

Figure 4. UV-ICE-based stretchable resistive sensors. (a) Illustration of a resistive sensor with the UV-ICE and nonconductive polymer. (b) Resistance response of the UV-ICE resistive sensor after being stretched. (c) The strain ε on the sensor and the force F applied to the sensor versus the relative resistance change $\Delta R/R_0$. (d) Photograph of a glove with strain sensors prepared by multimaterial 3D printing. Scale bar: 10 mm. (e) Photograph of the printed glove after transferring onto the hand. Scale bar: 10 mm. (f) Signal change as a function of time for strain sensors within the glove at different hand positions. Scale bar: 6 cm. (g) Stress−strain behavior of the matrix material with different Young's moduli. (h) $\Delta R/R_0$ of the resistive sensor versus the matrix material with different Young's moduli (d_1 = 0.3 mm, d_2 = 0.5 mm). (i) $\Delta R/R_0$ of the resistive sensor versus the matrix material with different thicknesses (E = 93 MPa, d_1 = 0.3 mm). (j) Variation of sensitivity and maximal measured force of the resistive sensor by tuning Young's modulus and thickness of the matrix.

Moreover, to improve the printing resolution, we choose Sudan I as the photo-absorber. As presented in Figure S10, the UV-ICE system with the photo-absorber requires more energy (longer time) to cure the same depth.

DLP-based multimaterial 3D printing is an ideal technology to fabricate ion-based flexible electronic devices consisting of UV-ICEs and other UV-curable polymers.[43] Figure 3d presents a printed Octet truss lattice structure printed with the UV-ICE and BA−AUD elastomer. The interfacial toughness between the UV-ICE and the (meth)acrylate polymer is the key to determining the mechanical performance of a printed structure. At the interface, the free radicals within the (meth)acrylate polymer combine with those unreacted monomers and oligomers within the UV-ICE domain, resulting in the chemical bonding between the (meth)acrylate-based polymer layer and the UV-ICE layer (Figure 3e,f). To further demonstrate the strong interfacial bonding, we prepared the dog bone samples printed with half UV-ICEs and half (meth)acrylate polymers for tensile testing (Figure 3g). As shown in Figure 3h, there was a firm interfacial bonding between UV-ICEs and other UV-curable elastomers including BA−AUD and three commercial elastomers (Agilus, Vero, and Tango from Stratasys Ltd.). We also performed the 180° peeling tests to investigate the interfacial toughness between UV-ICE and other UV-curable elastomers. As shown in Figure 3i, the interface toughness for the UV-ICE on the four different elastomers is 570−810 N/m, indicating that the UV-ICE is able to form robust interfaces with other UV-curable elastomers.

2.4. 3D Printing UV-ICE-Based Stretchable Resistive Sensors. The capability of printing UV-ICE with other polymers allows us to quickly fabricate resistive sensors that can monitor the changes in strain or force. Figure 4a presents the illustration of a resistive sensor where the UV-ICE circuit with thickness d_1 is embedded into a nonconductive polymer matrix with thickness d_2. As illustrated in Figure 4b, a tensile force F leads the sensor to be stretched by $(\Delta L + L_0)/L_0$ so that the resistance of the circuit increases from R_0 to $R_0 + \Delta R$. As shown in Figure 4c, according to the correlation between the relative resistance change $\Delta R/R_0$ and the strain ε ($\varepsilon = \Delta L/L_0$) on the sensor, the resistive sensor can be used as a strain sensor; by tuning Young's modulus E and cross-sectional area

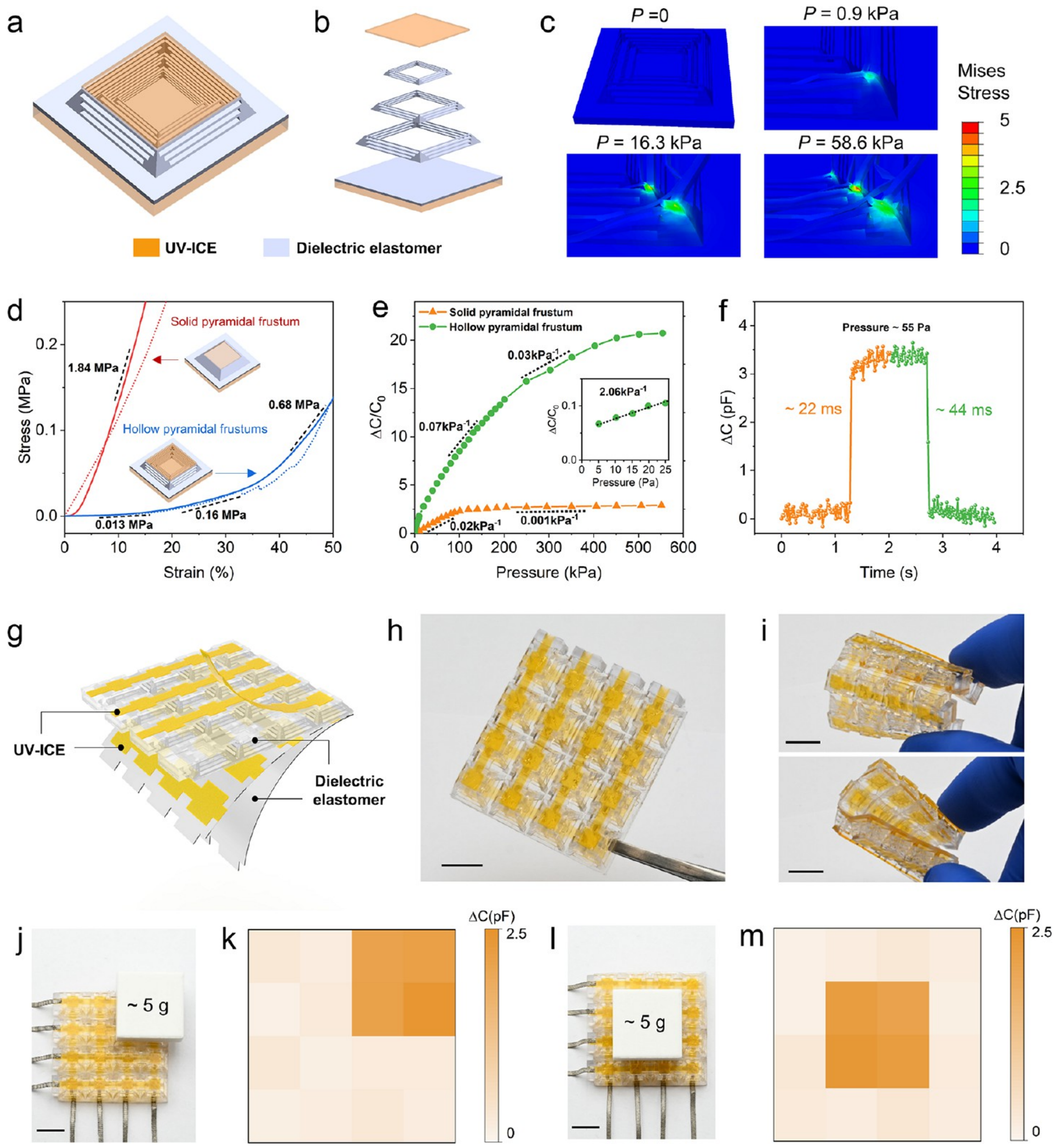

Figure 5. Multimaterial 3D printed capacitive pressure sensor with UV-ICE. (a) Schematic illustration of the capacitive pressure sensor. (b) The microstructure of the dielectric layer. (c) Stress distribution of the simulation results for the dielectric layer with three hollow pyramidal frustums under different pressures. (d) Compressive test of the dielectric layer (red curve, solid pyramidal frustum; blue curve, hollow pyramidal frustum; solid curve, experimental data; dashed curve, FEA simulated data). (e) Change of capacitance over the pressure range of up to 550 kPa. (f) Instant response of the pressure sensor. (g) Schematic illustrations of the flexible pressure sensor array. (h) Photograph showing the multimaterial printed pressure sensor array with 4 × 4 sensing pixels. Scale bar: 10 mm. (i) Demonstrations of the flexible 3D printed multimaterial array. Scale bar: 10 mm. (j−m) Response behaviors of the printed pressure sensor array when placing a 5 g object on the 4 row × 4 column pixels. Scale bar: 10 mm.

A of the matrix, the resistive sensor can be further used to detect force based on the correlation between the relative resistance change $\Delta R/R_0$ and the force F ($F = E \times A \times \Delta L/L_0$) applied to the sensor.

Figure 4d presents a multimaterial 3D printed smart glove where five strain sensors made of UV-ICE are embedded to the soft matrix made of the nonconductive BA−AUD elastomer with Young's modulus of 3 MPa. Compared with previous works,[44−47] the DLP-based multimaterial 3D printing approach greatly simplifies the fabrication process and only took us 5 min to fabricate such a glove. Thanks to the strong adhesion of the BA−AUD substrate, as shown in Figure 4e, the smart glove can be firmly attached to a hand. In Figure 4f, the smart glove was used to collect finger motion signals that control a robotic hand to perform different gestures in real time (Movie S1). As shown in Figure 4g, every slight bending of each finger can be quickly and accurately detected by the smart glove so that the robotic hand can rapidly respond to imitate the gestures of our hand. Details on the electromechanical performance of the strain sensor and the adhesion and biocompatibility of the matrix material are presented in Figures S11−S14, respectively.

The printed sensor can also be used to measure force by using a stiffer material print matrix. Figure 4g shows the stress−strain curves for four materials whose Young's modulus ranges from 3 to 630 MPa. In Figure 4h, the increase in

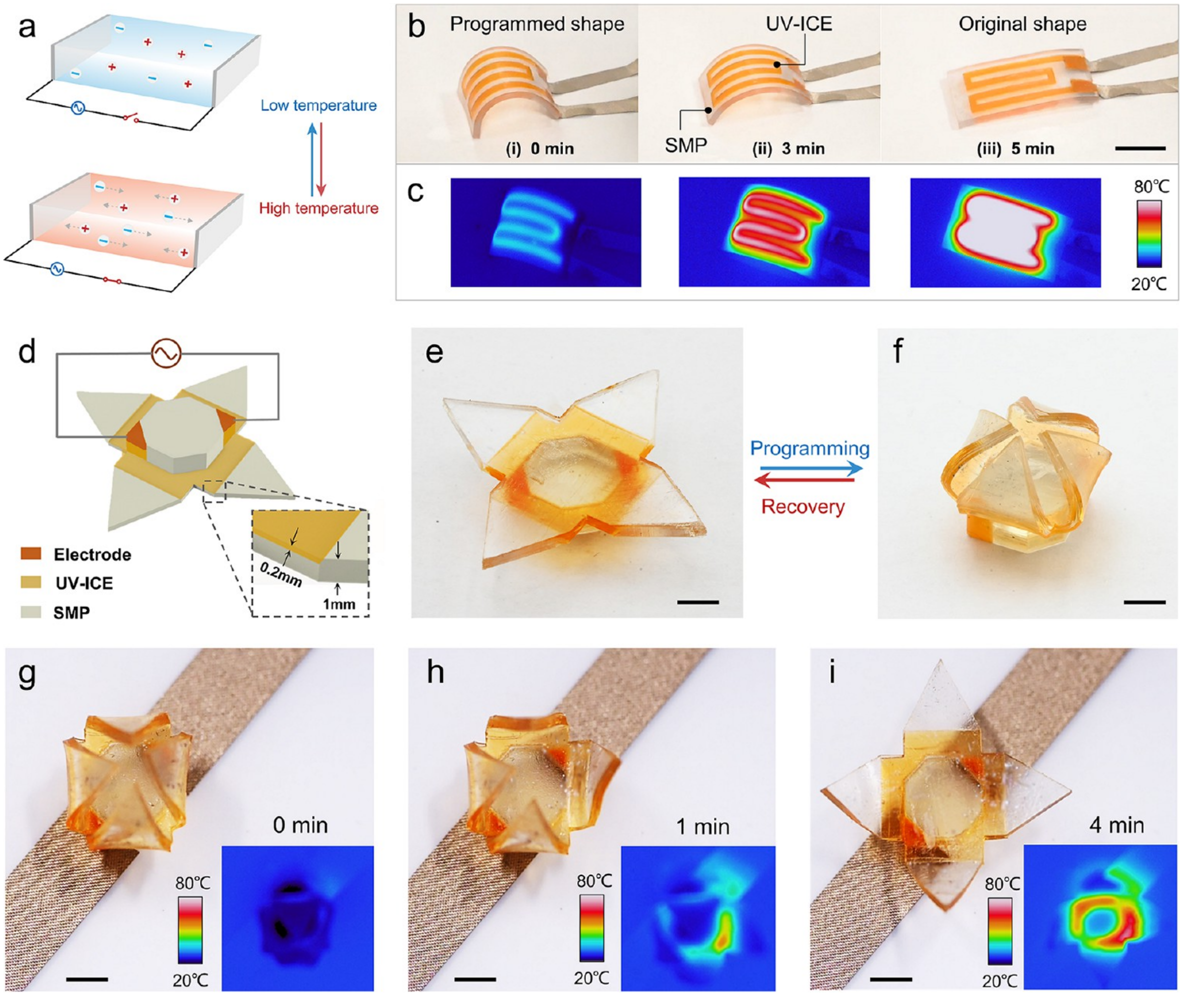

Figure 6. ICE-enabled 4D printing. (a) Schematic illustrations showing the generation of Joule heat in UV-ICE under a high-frequency alternative voltage. (b) Images showing the evolution of the bent SMP strip with the UV-ICE circuit under an applied alternative voltage ($V = 500$ V, $f = 1000$ Hz). Scale bar: 10 mm. (c) The corresponding thermal images for the cases in Figure 6b. (d) Illustrations on the design of an SMP flower with UV-ICE. (e) As-printed SMP flower with UV-ICE. Scale bar: 5 mm. (f) SMP flower with UV-ICE in a programmed compacted shape. Scale bar: 5 mm. (g−i) Images showing the development of the closed SMP flower with UV-ICE under an applied alternative voltage ($V = 200$ V, $f = 1000$ Hz). The inset pictures were corresponding thermal images. Scale bar: 5 mm.

Young's modulus of the matrix material leads to a higher force to achieve the same resistance change. For instance, to realize $\Delta R/R_0 = 0.4$, the applied force increases from 0.8 to 84 N by changing Young's modulus of the matrix material from 3 to 630 MPa. Moreover, we can tune the force−relative resistance change relation by changing the thickness of the matrix d_1. As demonstrated in Figure 4i, to realize $\Delta R/R_0 = 0.4$, the applied force increases from 20 to 61 N by changing d_2 from 0.5 to 3 mm. As summarized in Figure 4j, by tuning Young's modulus and thickness of the matrix, the printed sensor is able to measure a wide range of forces, but the sensitivity accordingly decreases with the increase in the magnitude of the measured force.

2.5. Multimaterial 3D Printed Capacitive Pressure Sensor with UV-ICE. The capability of printing UV-ICE with a dielectric elastomer also allows us to quickly fabricate flexible capacitive sensors to monitor pressure. The high-resolution multimaterial 3D printing allows us to directly print the dielectric layer with microstructures to achieve better performance of a pressure sensor. As shown in Figure 5a, we design a 3D printed capacitive pressure sensor where the dielectric layer is composed of three hollow pyramidal frustums with different sizes (dielectric layer: BA−AUD elastomer, 30 wt % AUD). Figure 5b presents the microstructure of the dielectric layer. Figure S15 shows the image of the printed dielectric layer with three hollow pyramidal frustums. We conducted finite element analysis (FEA) to simulate the compressive process of the dielectric layer. Details on FEA can be found in Experimental Section. As shown in Figure 5c, the three hollow pyramidal frustums gradually bend until all of them are compressed. As shown in Figure 5d, we performed a compressive test to investigate the stress−strain behavior of the dielectric layer with three hollow pyramidal frustums. When only the outer pyramidal frustum is compressed, the initial stiffness of the sensor is 0.013 MPa. Then, the stiffness turns to be 0.16 MPa, and 0.68 MPa after the middle and inner pyramidal frustums are sequentially compressed. In comparison, the solid pyramidal frustum exhibits a much higher stiffness of 1.84 MPa. Figure 5e presents the relative capacity change ($\Delta C/C_0$) over pressure P. The initial sensitivity S [$S = (\delta\Delta C/C_0)/\delta P$] of the sensor with three hollow pyramidal frustums is 2.06 kPa^{-1}. As shown in the inset of Figure 5e, the low stiffness of the hollow pyramidal frustums allows the sensor to measure an ultralow pressure of 5 Pa. The three hollow pyramidal frustums with different sizes extend the up limit of measured pressure to 550 kPa while maintaining a relatively high sensitivity ($S = 0.07$ kPa^{-1}). In comparison, the sensitivity of the sensor with a solid pyramidal frustum is only 0.02 kPa^{-1}, and the sensitivity decreases to 0.001 kPa^{-1} when the pressure is higher than 100 kPa due to the high stiffness and incompressibility of the solid pyramidal frustum. To demonstrate that the 3D printed sensors are able to detect an ultralow pressure with a fast response, as shown in Figure 5f, a weight of 0.12 g is gently placed on the pressure sensor and then quickly removed. The sensor detects the variation in capacitance by 2.9 pF within 22 ms, and the capacitance turns to the initial value within 44 ms.

Table S1 compares the performance of the 3D printed pressure sensor with that of previously reported ionic pressure sensors.[28,33,40,48−56] The pressure sensor in this work exhibits a broad detection range from 5 Pa to 500 kPa and a high sensitivity of 2.06 kPa^{-1}. More importantly, the pressure sensor in this work is fully 3D printed, which saves time of fabrication, especially in the case of fabricating a pressure sensor array. Figure 5g illustrates the design of the pressure sensor array composed of 4 × 4 sensor units. The pressure sensor array includes four layers: a nonconductive elastomeric substrate, two circuit layers, and a dielectric layer of hollow pyramidal frustums. In each circuit layer, there are four parallel UV-ICE bands. The UV-ICE bands in the two circuit layers are orthogonal to each other. Figure 5h presents the snapshot of the printed pressure sensor array that was directly printed within 15 min. Figure 5i demonstrates its excellent flexibility as all constituent materials are highly stretchable. Figure 5j−m demonstrates that the printed pressure sensor array is able to map the pressure distribution when a 5 g square is placed on two different locations of the sensor array.

2.6. ICE-Enabled 4D Printing.

Through multimaterial 3D printing UV-ICE into the SMP matrix, we can also realize electronically controlled, Joule heating activated 4D printing. As illustrated in Figure 6a, the application of a high-frequency alternative voltage ($V = 200{-}500$ V, $f = 1$ kHz) makes UV-ICE generate heat due to the fast motion of cations and anions. In Figure 6b, we printed a multimaterial straight strip where the UV-ICE circuit was embedded into the SMP matrix and programmed the strip into a bent shape. After applying an alternative voltage, the bent SMP strip gradually recovered into its original straight shape due to Joule heating for the UV-ICE circuit. Figure 6c presents the corresponding infrared images of the Joule heating process where the heat was generated from the UV-ICE circuit and gradually diffused to the entire SMP matrix. To further demonstrate the concept to UV-ICE circuit-activated 4D printing, Figure 6d presents the design of an SMP flower where the UV-ICE is placed at the four hinges as well as the two corners of its base that are connected to the alternative voltage supplier. Figure 6e,f shows the images of the flower in its open (as-printed) and close (programmed) configurations, respectively. As shown in Figure 6g−i and Movie S2, the opening process of the flower can be triggered by applying an alternative voltage ($V = 200$ V, $f = 1000$ Hz) on the UV-ICE circuit. The inset infrared images clearly show that the only parts connected with UV-ICE are heated to trigger the shape recovery of the SMP hinges.

3. CONCLUSIONS

We report a DLP-based multimaterial 3D printing capability to seemly integrate ICE with nonconductive materials to create ionic flexible electronic devices in 3D forms. We develop UV-ICEs that are highly stretchable and compatible with DLP-based 3D printing to create highly complex ionic conductive 3D structures with high resolution. The UV-ICEs are able to form a mechanically robust interface with other UV-curable but nonconductive materials ranging from soft elastomers to rigid polymers. This unique capability allows us to use a self-built DLP-based multimaterial 3D printer to readily manufacture various flexible electronic devices consisting of ICE-based circuits and various nonconductive polymers. To demonstrate this, we printed UV-ICE circuits into polymer substrates with different mechanical properties to create resistive strain and force sensors; we printed flexible capacitive sensors with high sensitivity and a wide range of measured pressures by creating a complex microstructure in the dielectric layer; we even realized ionic conductor-activated 4D printing by embedding a UV-ICE circuit into a shape memory polymer substrate.

4. EXPERIMENTAL SECTION

4.1. Materials.

BA, acrylamide (AAm), and Sudan I were purchased from Aladdin (China). AUD (Ebecryl 8413) was kindly provided by Allnex (Germany). Diphenyl(2,4,6-trimethylbenzoyl) phosphine oxide (TPO) and lithium bis(trifluoromethane sulfonimide) (LiTFSI) were purchased from Bide (China). Poly(ethylene glycol) diacrylate (PEGDA; $M_n = 700$) were purchased from Sigma-Aldrich (China).

4.2. Preparation of UV-ICE.

UV-ICEs were fabricated by photopolymerization. First, AUD, TPO, and LiTFSI were dissolved in the BA−AUD mixture (BA/AUD = 8:2 w/w), forming a transparent precursor solution. The mass percentage of TPO to BA was 1 wt %. The content of LiTFSI was fixed at 10, 20, 30, 40, and 50 wt %. In some cases, 0.05 wt % Sudan I of the total weight of the solution was used. Then, the solution was injected into a polytetrafluoroethylene mold. UV-ICE was cured in 5 min by UV light irradiation (wavelength 365 nm).

4.3. Preparation of the PAAm Hydrogel.

The PAAm hydrogel made of 80 wt % water and a 20 wt % acrylamide−PEGDA mixture with a PEGDA/acrylamide mixing ratio of 0.625 wt % were prepared. The self-prepared water-soluble photoinitiator 2,4,6-trimethylbenzoyl diphenylphosphine oxide (TPO) at 0.5 wt % acrylamide was added into water. The water-soluble TPO is now also commercially available and can be directly purchased from Sigma-Aldrich (product nos. 906808 and 906816).

4.4. 3D Printing.

The grid pattern in Figure 3a was printed using a commercial 3D printer (405 nm, nanoArch S130, BMF Precision Technology Co., China). The Octet truss structure in Figure 3b was printed using a commercial 3D printer (405 nm, nanoArch S240, BMF Precision Technology Co., China). The other printed structures were printed on a self-built 3D printer with 405 nm UV light.

4.5. Mechanical Tests.

The test was carried out by using samples with a dimension of 15 mm × 5 mm × 1 mm under a 10 mm/min strain rate. The tests were performed on an MTS uniaxial tensile testing machine (Criterion Model 43) with a 100 N load cell.

4.6. FTIR Spectroscopy.

The FTIR spectra were recorded using an FTIR spectrophotometer (Thermo Nicolet iS50) from 400 to 4000 cm^{-1}.

4.7. Electrical Characterization.

The impedance−frequency tests were performed on an electrochemical workstation (CHI660E). The conductivity of the UV-ICE was then calculated by $\sigma = L/(SR)$, where L is the distance between the electrodes, S is the cross-sectional area of the sample, and R the bulk resistance measured by the multimeter. The bulk resistance of the samples was measured by a precision LCR meter (TH2838H, test frequency: 1 kHz).

4.8. DSC Measurements.

The measurements were performed on a differential scanning calorimeter (TA DSC2500) via a scanning rate of 10 °C/min from −80 to 100 °C under flowing N_2.

4.9. TGA Measurements. The measurements were performed on a thermal gravimetric analyzer (TG 209F1) via a scanning rate of 10 °C/min from 35 to 700 °C under flowing N_2.

4.10. Rheological Measurements. The viscosity of all UV-ICE samples was measured by using a rheometer (TA DHR3) with a parallel plate geometry (diameter 20 mm, gap 200 μm). The gel point and storage modulus of all UV-ICE samples were measured using a rheometer (TA DHR3) with a parallel plate geometry (diameter 20 mm, gap 100 μm) to characterize the transition process from solution to gel by UV irradiation. To perform these experiments, a UV light source (405 nm, 8.4 mW/cm^2) was attached to the rheometer.

4.11. Curing Thickness. First, the prepared UV-ICE precursor solutions were sandwiched between two glass slides with a gap from 50 to 200 μm, and then the patterned near UV light (405 nm, 19.34 mW/cm^2) was irradiated. The curing time was recorded when a pattern could be visually observed.

4.12. 180° Peeling Tests. The tests were performed on an MTS uniaxial tensile testing machine (Criterion Model 43) with a 100 N load cell. Both the UV-ICE and dielectric elastomers were attached to the backing layer (PET film) to constrain deformation. The UV-ICE and dielectric elastomer are bonded in an area of 30 mm × 15 mm. The tests were conducted at a constant peeling speed of 10 mm/min.

4.13. FEA. To predict the deformation on the hollow pyramidal frustums, FEA simulations were conducted by using the commercially available software package ABAQUS ((V6.14, Dassault Systèmes Simulia Corp., USA). We use the hyperelastic Mooney−Rivlin model with strain energy density function to describe the nonlinear material behavior of Agilus (Stratasys Ltd.). The material coefficients were set as C10 = 0.224 MPa, C01 = −0.189 MPa, and D1 = 0.001 MPa, which were obtained by fitting the uniaxial tensile experiments of Agilus. The 3D model of the hollow pyramidal frustums was constructed and analyzed on ABAQUS/Explicit (Simulia, Dassault Systèmes). The solid tetrahedron quadratic element (element type C3D10M) was used to mesh the structures. The displacement was applied to the rigid plate above the hollow pyramidal frustums to simulate the quasi-static compression.

■ ASSOCIATED CONTENT

SI Supporting Information

The Supporting Information is available free of charge at https://pubs.acs.org/doi/10.1021/acsami.2c18954.

> Characterizations of the UV-ICE and BA−AUD elastomer; viscosity of precursor solution; characterization of UV-curing behavior of precursor solution; resistance response of the UV-ICE strain sensor; adhesion of the BA−AUD elastomer; biocompatibility test of the BA−AUD elastomer; and the image of the printed dielectric layer with three hollow pyramidal frustums (PDF)
>
> Movie of controlling a robotic hand to perform different gestures with a 3D printing smart glove (Movie S1) (MP4)
>
> The near-infrared imaging of the opening process of the SMP flower under an alternative voltage (V = 200 V, f = 1000 Hz) (Movie S2) (MP4)

■ AUTHOR INFORMATION

Corresponding Author

Qi Ge − *Shenzhen Key Laboratory of Soft Mechanics & Smart Manufacturing, Southern University of Science and Technology, Shenzhen 518055, China; Department of Mechanical and Energy Engineering, Southern University of Science and Technology, Shenzhen 518055, China;* orcid.org/0000-0002-8666-8532; Email: geq@sustech.edu.cn

Authors

Xiangnan He − *Shenzhen Key Laboratory of Soft Mechanics & Smart Manufacturing, Southern University of Science and Technology, Shenzhen 518055, China; Department of Mechanical and Energy Engineering, Southern University of Science and Technology, Shenzhen 518055, China*

Jianxiang Cheng − *Shenzhen Key Laboratory of Soft Mechanics & Smart Manufacturing, Southern University of Science and Technology, Shenzhen 518055, China; Department of Mechanical and Energy Engineering, Southern University of Science and Technology, Shenzhen 518055, China*

Zhenqing Li − *Shenzhen Key Laboratory of Soft Mechanics & Smart Manufacturing, Southern University of Science and Technology, Shenzhen 518055, China; Department of Mechanical and Energy Engineering, Southern University of Science and Technology, Shenzhen 518055, China*

Haitao Ye − *Shenzhen Key Laboratory of Soft Mechanics & Smart Manufacturing, Southern University of Science and Technology, Shenzhen 518055, China; Department of Mechanical and Energy Engineering, Southern University of Science and Technology, Shenzhen 518055, China*

Xinfeng Wei − *Shenzhen Key Laboratory of Soft Mechanics & Smart Manufacturing, Southern University of Science and Technology, Shenzhen 518055, China; Department of Mechanical and Energy Engineering, Southern University of Science and Technology, Shenzhen 518055, China*

Honggeng Li − *Shenzhen Key Laboratory of Soft Mechanics & Smart Manufacturing, Southern University of Science and Technology, Shenzhen 518055, China; Department of Mechanical and Energy Engineering, Southern University of Science and Technology, Shenzhen 518055, China*

Rong Wang − *Shenzhen Key Laboratory of Soft Mechanics & Smart Manufacturing, Southern University of Science and Technology, Shenzhen 518055, China; Department of Mechanical and Energy Engineering, Southern University of Science and Technology, Shenzhen 518055, China*

Yuan-Fang Zhang − *Shien-Ming Wu School of Intelligent Engineering, South China University of Technology, Guangzhou 511442, China;* orcid.org/0000-0002-2903-9027

Hui Ying Yang − *Digital Manufacturing and Design Centre, Singapore University of Technology and Design, Singapore 487372, Singapore;* orcid.org/0000-0002-2244-8231

Chuanfei Guo − *Department of Materials Science and Engineering, Southern University of Science and Technology, Shenzhen 518055, China*

Complete contact information is available at: https://pubs.acs.org/10.1021/acsami.2c18954

Author Contributions

[#]X.H. and J.C. contributed equally to this work. X.H., J.C., and Q.G. conceived the ideas and designed the research. X.H. synthesized the materials and carried out experiments. J.C. designed and fabricated multimaterial 3D flexible electronics. X.H., J.C., and Z.L. demonstrated the applications. H.Y. and X.W. helped the structural design. H.L. and R.W. assisted 3D printing. Y.-F.Z., H.Y.Y., and C.G. participated in the discussion of the experimental results. X.H. drafted the manuscript. X.H. and Q.G. revised the manuscript.

Notes

The authors declare no competing financial interest.

■ ACKNOWLEDGMENTS

We acknowledge the support from the National Key Research and Development Program of China (no. 2020YFB1312900), the Science, Technology and Innovation Program (grant no. 20009618, The Development of PAD Printer System for Micro LED Multi-Bonding Technology) funded by the Ministry of Trade, Industry & Energy (MOTIE, Korea), the Science, Technology and Innovation Commission of Shenzhen Municipality under grant no. ZDSYS20210623092005017, and the Centers for Mechanical Engineering Research and Education at MIT and SUSTech. Y.-F.Z. and H.Y.Y. acknowledge the support by the Agency for Science, Technology and Research (A*STAR, Singapore) AME Programmatic Funding Scheme [A18A1b0045].

■ REFERENCES

(1) Wang, S.; Xu, J.; Wang, W.; Wang, G.-J. N.; Rastak, R.; Molina-Lopez, F.; Chung, J. W.; Niu, S.; Feig, V. R.; Lopez, J.; Lei, T.; Kwon, S. K.; Kim, Y.; Foudeh, A. M.; Ehrlich, A.; Gasperini, A.; Yun, Y.; Murmann, B.; Tok, J. B.; Bao, Z. Skin Electronics from Scalable Fabrication of an Intrinsically Stretchable Transistor Array. *Nature* **2018**, *555*, 83−88.

(2) Xu, J.; Wang, S.; Wang, G.-J. N.; Zhu, C.; Luo, S.; Jin, L.; Gu, X.; Chen, S.; Feig, V. R.; To, J. W. F.; Rondeau-Gagné, S.; Park, J.; Schroeder, B. C.; Lu, C.; Oh, J. Y.; Wang, Y.; Kim, Y.-H.; Yan, H.; Sinclair, R.; Zhou, D.; Xue, G.; Murmann, B.; Linder, C.; Cai, W.; Tok, J. B.-H.; Chung, J. W.; Bao, Z. Highly Stretchable Polymer-semiconductor Films through Thenanoconfinement Effect. *Science* **2017**, *355*, 59−64.

(3) Yang, R.; Qin, Y.; Dai, L.; Wang, Z. L. Power Generation with Laterally Packaged Piezoelectric Fine Wires. *Nat. Nanotechnol.* **2009**, *4*, 34−39.

(4) Persano, L.; Dagdeviren, C.; Su, Y.; Zhang, Y.; Girardo, S.; Pisignano, D.; Huang, Y.; Rogers, J. A. High Performance Piezoelectric Devices Based on Aligned Arrays of Nanofibers of Poly(Vinylidenefluoride-Co-Trifluoroethylene). *Nat. Commun.* **2013**, *4*, 1633.

(5) Lee, S.; Reuveny, A.; Reeder, J.; Lee, S.; Jin, H.; Liu, Q.; Yokota, T.; Sekitani, T.; Isoyama, T.; Abe, Y.; Suo, Z.; Someya, T. A Transparent Bending-Insensitive Pressure Sensor. *Nat. Nanotechnol.* **2016**, *11*, 472−478.

(6) Kaltenbrunner, M.; Sekitani, T.; Reeder, J.; Yokota, T.; Kuribara, K.; Tokuhara, T.; Drack, M.; Schwödiauer, R.; Graz, I.; Bauer-Gogonea, S.; Bauer, S.; Someya, T. An Ultra-Lightweight Design for Imperceptible Plastic Electronics. *Nature* **2013**, *499*, 458−463.

(7) Chung, H. U.; Rwei, A. Y.; Hourlier-Fargette, A.; Xu, S.; Lee, K.; Dunne, E. C.; Xie, Z.; Liu, C.; Carlini, A.; Kim, D. H.; Ryu, D.; Kulikova, E.; Cao, J.; Odland, I. C.; Fields, K. B.; Hopkins, B.; Banks, A.; Ogle, C.; Grande, D.; Park, J. B.; Kim, J.; Irie, M.; Jang, H.; Lee, J.; Park, Y.; Kim, J.; Jo, H. H.; Hahm, H.; Avila, R.; Xu, Y.; Namkoong, M.; Kwak, J. W.; Suen, E.; Paulus, M. A.; Kim, R. J.; Parsons, B. V.; Human, K. A.; Kim, S. S.; Patel, M.; Reuther, W.; Kim, H. S.; Lee, S. H.; Leedle, J. D.; Yun, Y.; Rigali, S.; Son, T.; Jung, I.; Arafa, H.; Soundararajan, V. R.; Ollech, A.; Shukla, A.; Bradley, A.; Schau, M.; Rand, C. M.; Marsillio, L. E.; Harris, Z. L.; Huang, Y.; Hamvas, A.; Paller, A. S.; Weese-Mayer, D. E.; Lee, J. Y.; Rogers, J. A. Skin-Interfaced Biosensors for Advanced Wireless Physiological Monitoring in Neonatal and Pediatric Intensive-Care Units. *Nat. Med.* **2020**, *26*, 418−429.

(8) Park, S. I.; Brenner, D. S.; Shin, G.; Morgan, C. D.; Copits, B. A.; Chung, H. U.; Pullen, M. Y.; Noh, K. N.; Davidson, S.; Oh, S. J.; Yoon, J.; Jang, K. I.; Samineni, V. K.; Norman, M.; Grajales-Reyes, J. G.; Vogt, S. K.; Sundaram, S. S.; Wilson, K. M.; Ha, J. S.; Xu, R.; Pan, T.; Kim, T. I.; Huang, Y.; Montana, M. C.; Golden, J. P.; Bruchas, M. R.; Gereau, R. W. t.; Rogers, J. A. Soft, Stretchable, Fully Implantable Miniaturized Optoelectronic Systems for Wireless Optogenetics. *Nat. Biotechnol.* **2015**, *33*, 1280−1286.

(9) Xu, L.; Gutbrod, S. R.; Bonifas, A. P.; Su, Y.; Sulkin, M. S.; Lu, N.; Chung, H. J.; Jang, K. I.; Liu, Z.; Ying, M.; Lu, C.; Webb, R. C.; Kim, J. S.; Laughner, J. I.; Cheng, H.; Liu, Y.; Ameen, A.; Jeong, J. W.; Kim, G. T.; Huang, Y.; Efimov, I. R.; Rogers, J. A. 3d Multifunctional Integumentary Membranes for Spatiotemporal Cardiac Measurements and Stimulation across the Entire Epicardium. *Nat. Commun.* **2014**, *5*, 3329.

(10) Wehner, M.; Truby, R. L.; Fitzgerald, D. J.; Mosadegh, B.; Whitesides, G. M.; Lewis, J. A.; Wood, R. J. An Integrated Design and Fabrication Strategy for Entirely Soft, Autonomous Robots. *Nature* **2016**, *536*, 451−455.

(11) Wang, Y.; Zhu, C.; Pfattner, R.; Yan, H.; Jin, L.; Chen, S.; Molina-Lopez, F.; Lissel, F.; Liu, J.; Rabiah, N. I.; Chen, Z.; Chung, J. W.; Linder, C.; Toney, M. F.; Murmann, B.; Bao, Z. A Highly Stretchable, Transparent,and Conductive Polymer. *Sci. Adv.* **2017**, *3*, e1602076.

(12) Kim, D.-H.; Ahn, J.-H.; Choi, W. M.; Kim, H.-S.; Kim, T.-H.; Song, J.; Huang, Y. Y.; Liu, Z.; Lu, C.; Rogers, J. A. Stretchable and Foldable Siliconintegrated Circuits. *Science* **2008**, 320.

(13) Kim, D.-H.; Song, J.; Choi, W. M.; Kim, H.-S.; Kim, R.-H.; Liu, Z.; Huang, Y. Y.; Hwang, K.-C.; Zhang, Y.-w.; Rogers, J. A. Materials and Noncoplanar Mesh Designs for Integrated Circuits with Linear Elastic Responses to Extreme Mechanical Deformations. *Proc. Natl. Acad. Sci.* **2008**, *105*, 18675−18680.

(14) Shyu, T. C.; Damasceno, P. F.; Dodd, P. M.; Lamoureux, A.; Xu, L.; Shlian, M.; Shtein, M.; Glotzer, S. C.; Kotov, N. A. A Kirigami Approach to Engineering Elasticity in Nanocomposites through Patterned Defects. *Nat. Mater.* **2015**, *14*, 785−789.

(15) Chun, K. Y.; Oh, Y.; Rho, J.; Ahn, J. H.; Kim, Y. J.; Choi, H. R.; Baik, S. Highly Conductive, Printable and Stretchable Composite Films of Carbon Nanotubes and Silver. *Nat. Nanotechnol.* **2010**, *5*, 853−857.

(16) Tybrandt, K.; Vörös, J. Fast and Efficient Fabrication of Intrinsically Stretchable Multilayer Circuit Boards by Wax Pattern Assisted Filtration. *Small* **2016**, *12*, 180−184.

(17) Kim, Y.; Zhu, J.; Yeom, B.; Di Prima, M.; Su, X.; Kim, J. G.; Yoo, S. J.; Uher, C.; Kotov, N. A. Stretchable Nanoparticle Conductors with Self-Organized Conductive Pathways. *Nature* **2013**, *500*, 59−63.

(18) Matsuhisa, N.; Kaltenbrunner, M.; Yokota, T.; Jinno, H.; Kuribara, K.; Sekitani, T.; Someya, T. Printable Elastic Conductors with a High Conductivity for Electronic Textile Applications. *Nat. Commun.* **2015**, *6*, 7461.

(19) Keplinger, C.; Sun, J.-Y.; Foo, C. C.; Rothemund, P.; Whitesides, G. M.; Suo, Z. Stretchable, Transparent, Ionic Conductors. *Science* **2013**, 341.

(20) Kim, H. J.; Chen, B.; Suo, Z.; Hayward, R. C. Ionoelastomer Junctions between Polymer Networks of Fixed Anions and Cations. *Science* **2020**, *367*, 773−776.

(21) Yang, C.; Suo, Z. Hydrogel Ionotronics. *Nat. Rev. Mater.* **2018**, *3*, 125−142.

(22) Dong, L.; Agarwal, A. K.; Beebe, D. J.; Jiang, H. Adaptive Liquid Microlenses Activated by Stimuli-Responsive Hydrogels. *Nature* **2006**, *442*, 551−554.

(23) Liu, Y.; Liu, J.; Chen, S.; Lei, T.; Kim, Y.; Niu, S.; Wang, H.; Wang, X.; Foudeh, A. M.; Tok, J. B.-H.; Bao, Z. Soft and Elastic Hydrogel-Based Microelectronics for Localized Low-Voltage Neuromodulation. *Nat. Biomed. Eng.* **2019**, *3*, 58−68.

(24) Kim, C.-C.; Lee, H.-H.; Oh, K. H.; Sun, J.-Y. Highly Stretchable, Transparent Ionic Touch Panel. *Science* **2016**, 353.

(25) Schroeder, T. B. H.; Guha, A.; Lamoureux, A.; VanRenterghem, G.; Sept, D.; Shtein, M.; Yang, J.; Mayer, M. An Electric-Eel-Inspired Soft Power Source from Stacked Hydrogels. *Nature* **2017**, *552*, 214−218.

(26) Yuk, H.; Lin, S.; Ma, C.; Takaffoli, M.; Fang, N. X.; Zhao, X. Hydraulic Hydrogel Actuators and Robots Optically and Sonically Camouflaged in Water. *Nat. Commun.* **2017**, *8*, 14230.

(27) Li, T.; Li, G.; Liang, Y.; Cheng, T.; Dai, J.; Yang, X.; Liu, B.; Zeng, Z.; Huang, Z.; Luo, Y.; Xie, T.; Yang, W. Fast-Moving Soft Electronic Fish. *Sci. Adv.* **2017**, *3*, e1602045.

(28) Sun, J. Y.; Keplinger, C.; Whitesides, G. M.; Suo, Z. Ionic Skin. *Adv. Mater.* **2014**, *26*, 7608−7614.

(29) Yuk, H.; Zhang, T.; Parada, G. A.; Liu, X.; Zhao, X. Skin-Inspired Hydrogel-Elastomer Hybrids with Robust Interfaces and Functional Microstructures. *Nat. Commun.* **2016**, *7*, 12028.

(30) Pu, X.; Liu, M.; Chen, X.; Sun, J.; Du, C.; Zhang, Y.; Zhai, J.; Hu, W.; Wang, Z. L. Ultrastretchable, Transparent Triboelectricnanogenerator as Electronic Skin for Biomechanicalenergy Harvesting and Tactile Sensing. *Sci. Adv.* **2017**, *2017*, e1700015.

(31) Shi, L.; Zhu, T.; Gao, G.; Zhang, X.; Wei, W.; Liu, W.; Ding, S. Highly Stretchable and Transparent Ionic Conducting Elastomers. *Nat. Commun.* **2018**, *9*, 2630.

(32) Lei, Z.; Wu, P. A Highly Transparent and Ultra-Stretchable Conductor with Stable Conductivity During Large Deformation. *Nat. Commun.* **2019**, *10*, 3429.

(33) Zhang, C.; Zheng, H.; Sun, J.; Zhou, Y.; Xu, W.; Dai, Y.; Mo, J.; Wang, Z. 3d Printed, Solid-State Conductive Ionoelastomer as a Generic Building Block for Tactile Applications. *Adv. Mater.* **2021**, e2105996.

(34) Shi, L.; Jia, K.; Gao, Y.; Yang, H.; Ma, Y.; Lu, S.; Gao, G.; Bu, H.; Lu, T.; Ding, S. Highly Stretchable and Transparent Ionic Conductor with Novel Hydrophobicity and Extreme-Temperature Tolerance. *Research* **2020**, *2020*, 1−10.

(35) Yiming, B.; Guo, X.; Ali, N.; Zhang, N.; Zhang, X.; Han, Z.; Lu, Y.; Wu, Z.; Fan, X.; Jia, Z.; Qu, S. Ambiently and Mechanically Stable Ionogels for Soft Ionotronics. *Adv. Funct. Mater.* **2021**, *31*, 2102773.

(36) Cao, Y.; Tan, Y. J.; Li, S.; Lee, W. W.; Guo, H.; Cai, Y.; Wang, C.; Tee, B. C. K. Self-Healing Electronic Skins for Aquatic Environments. *Nat. Electron.* **2019**, *2*, 75−82.

(37) Zhang, P.; Guo, W.; Guo, Z. H.; Ma, Y.; Gao, L.; Cong, Z.; Zhao, X. J.; Qiao, L.; Pu, X.; Wang, Z. L. Dynamically Crosslinked Dry Ion-Conducting Elastomers for Soft Iontronics. *Adv. Mater.* **2021**, e2101396.

(38) Cai, X.; Ye, B.; Ding, J.; Chi, Z.; Sun, L.; Saha, P.; Wang, G. Dual Li-Ion Migration Channels in an Ester-Rich Copolymer/Ionic Liquid Quasi-Solid-State Electrolyte for High-Performance Li−S Batteries. *J. Mater. Chem. A* **2021**, *9*, 2459−2469.

(39) Chen, X.; Bai, Y. K.; Zhao, C. Z.; Shen, X.; Zhang, Q. Lithium Bonds in Lithium Batteries. *Am. Ethnol.* **2020**, *59*, 11192−11195.

(40) Yiming, B.; Han, Y.; Han, Z.; Zhang, X.; Li, Y.; Lian, W.; Zhang, M.; Yin, J.; Sun, T.; Wu, Z.; Li, T.; Fu, J.; Jia, Z.; Qu, S. A Mechanically Robust and Versatile Liquid-Free Ionic Conductive Elastomer. *Adv. Mater.* **2021**, *33*, e2006111.

(41) Cheng, S.; Narang, Y. S.; Yang, C.; Suo, Z.; Howe, R. D. Stick-on Large-Strain Sensors for Soft Robots. *Adv. Mater. Interfaces* **2019**, *6*, 1900985.

(42) Zhang, B.; Li, H.; Cheng, J.; Ye, H.; Sakhaei, A. H.; Yuan, C.; Rao, P.; Zhang, Y. F.; Chen, Z.; Wang, R.; He, X.; Liu, J.; Xiao, R.; Qu, S.; Ge, Q. Mechanically Robust and Uv-Curable Shape-Memory Polymers for Digital Light Processing Based 4d Printing. *Adv. Mater.* **2021**, *33*, e2101298.

(43) Ge, Q.; Chen, Z.; Cheng, J.; Zhang, B.; Zhang, Y.-F.; Li, H.; He, X.; Yuan, C.; Liu, J.; Magdassi, S.; Qu, S. 3d Printing of Highly Stretchable Hydrogel with Diverse Uv Curable Polymers. *Sci. Adv.* **2021**, *7*, eaba4261.

(44) Gu, G.; Xu, H.; Peng, S.; Li, L.; Chen, S.; Lu, T.; Guo, X. Integrated Soft Ionotronic Skin with Stretchable and Transparent Hydrogel-Elastomer Ionic Sensors for Hand-Motion Monitoring. *Soft Rob.* **2019**, *6*, 368−376.

(45) Tang, L.; Shang, J.; Jiang, X. Multilayered Electronic Transfer Tattoo That Can Enable the Crease Amplification Effect. *Sci. Adv.* **2021**, *7*, eabe3778.

(46) Wu, Y.; Zeng, Y.; Chen, Y.; Li, C.; Qiu, R.; Liu, W. Photocurable 3d Printing of High Toughness and Self-Healing Hydrogels for Customized Wearable Flexible Sensors. *Adv. Funct. Mater.* **2021**, *31*, 2107202.

(47) Muth, J. T.; Vogt, D. M.; Truby, R. L.; Mengüç, Y.; Kolesky, D. B.; Wood, R. J.; Lewis, J. A. Embedded 3d Printing of Strain Sensors within Highly Stretchable Elastomers. *Adv. Mater.* **2014**, *26*, 6307−6312.

(48) Ren, Y.; Liu, Z.; Jin, G.; Yang, M.; Shao, Y.; Li, W.; Wu, Y.; Liu, L.; Yan, F. Electric-Field-Induced Gradient Ionogels for Highly Sensitive, Broad-Range-Response, and Freeze/Heat-Resistant Ionic Fingers. *Adv. Mater.* **2021**, *33*, e2008486.

(49) Amoli, V.; Kim, J. S.; Jee, E.; Chung, Y. S.; Kim, S. Y.; Koo, J.; Choi, H.; Kim, Y.; Kim, D. H. A Bioinspired Hydrogen Bond-Triggered Ultrasensitive Ionic Mechanoreceptor Skin. *Nat. Commun.* **2019**, *10*, 4019.

(50) Shen, Z.; Zhu, X.; Majidi, C.; Gu, G. Cutaneous Ionogel Mechanoreceptors for Soft Machines, Physiological Sensing, and Amputee Prostheses. *Adv. Mater.* **2021**, *33*, e2102069.

(51) Lei, Z.; Wang, Q.; Sun, S.; Zhu, W.; Wu, P. A Bioinspired Mineral Hydrogel as a Self-Healable, Mechanically Adaptable Ionic Skin for Highly Sensitive Pressure Sensing. *Adv. Mater.* **2017**, *29*, 1700321.

(52) Yin, X. Y.; Zhang, Y.; Xiao, J.; Moorlag, C.; Yang, J. Monolithic Dual-Material 3d Printing of Ionic Skins with Long-Term Performance Stability. *Adv. Funct. Mater.* **2019**, *29*, 1904716.

(53) Yin, X.-Y.; Zhang, Y.; Cai, X.; Guo, Q.; Yang, J.; Wang, Z. L. 3d Printing of Ionic Conductors for High-Sensitivity Wearable Sensors. *Mater. Horiz.* **2019**, *6*, 767−780.

(54) Lei, Z.; Wu, P. Adaptable Polyionic Elastomers with Multiple Sensations and Entropy-Driven Actuations for Prosthetic Skins and Neuromuscular Systems. *Mater. Horiz.* **2019**, *6*, 538−545.

(55) Xie, W.; Duan, J.; Wang, H.; Li, J.; Liu, R.; Yu, B.; Liu, S.; Zhou, J. Ultra-Stretchable, Bio-Inspired Ionic Skins That Work Stably in Various Harsh Environments. *J. Mater. Chem. A* **2018**, *6*, 24114−24119.

(56) Zhang, W.; Wu, B.; Sun, S.; Wu, P. Skin-Like Mechanoresponsive Self-Healing Ionic Elastomer from Supramolecular Zwitterionic Network. *Nat. Commun.* **2021**, *12*, 4082.